Supplemental Information

Diagonally Scanned Light-Sheet Microscopy for Fast Volumetric Imaging of Adherent Cells

Kevin M. Dean, Philippe Roudot, Carlos R. Reis, Erik S. Welf, Marcel Mettlen, and Reto Fiolka

Supporting Material

Diagonally Scanned Light-Sheet Microscopy for Fast Volumetric Imaging of Adherent Cells

Kevin M. Dean,[1,2] Philippe Roudot,[1,2] Carlos R. Reis,[2] Erik S. Welf,[1,2] Marcel Mettlen,[2] and Reto Fiolka[2,*]

[1]Lyda Hill Department of Bioinformatics and [2]Department of Cell Biology, University of Texas Southwestern Medical Center, Dallas, Texas

*Correspondence: reto.fiolka@utsouthwestern.edu
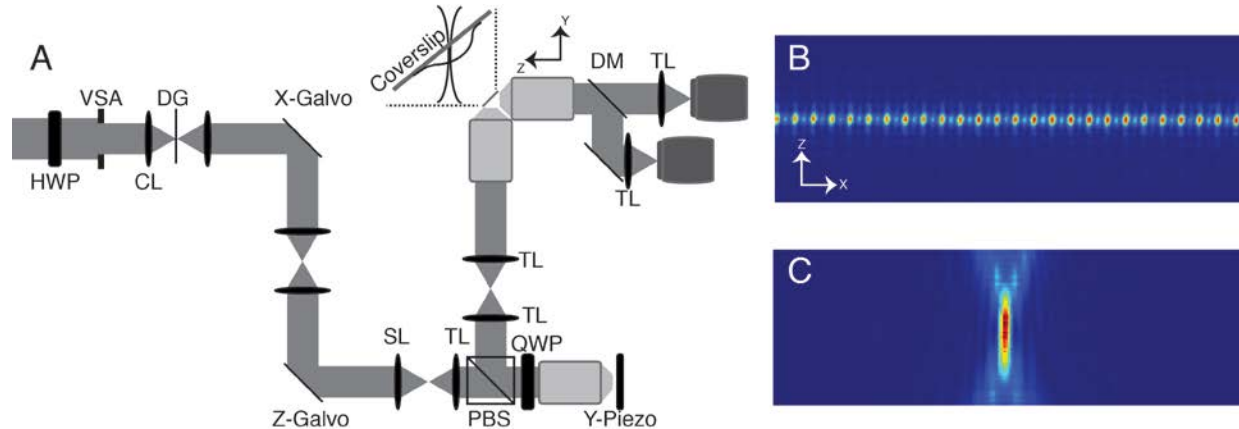
Supporting Figures:

Figure S1. (A) Technical drawing of microscope. HWP: half-waveplate, VSA: variable slit aperture, CL: cylindrical lens, DG: diffraction grating, SL: scan lens, TL: tube lens, PBS: polarizing beam splitter, QWP: quarter wave plate, DM: dichroic mirror. The coverslip, oriented at 45 degrees, is placed at the focal plane of both the excitation and detection objectives. Magnified view provides orientation of coverslip and cell within the context of the overall microscope design. (B) Gaussian lattice as observed in the intermediate image plane between the remote and excitation objective. (C) Axial cross-section, summed over one period, of the Gaussian lattice.
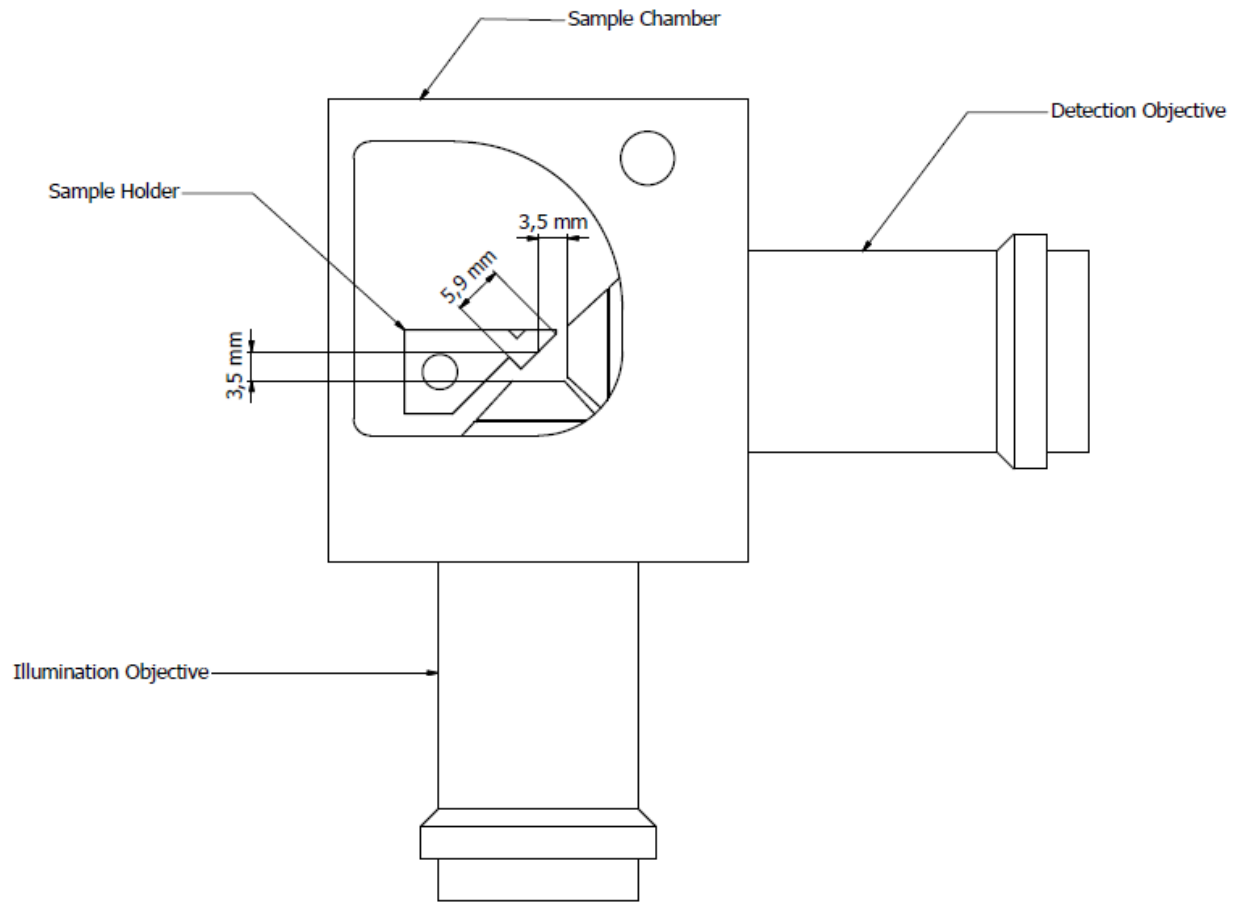
v

Figure S2. CAD drawing of the sample mounting inside the sample chamber and clearance to the illumination and detection objective.
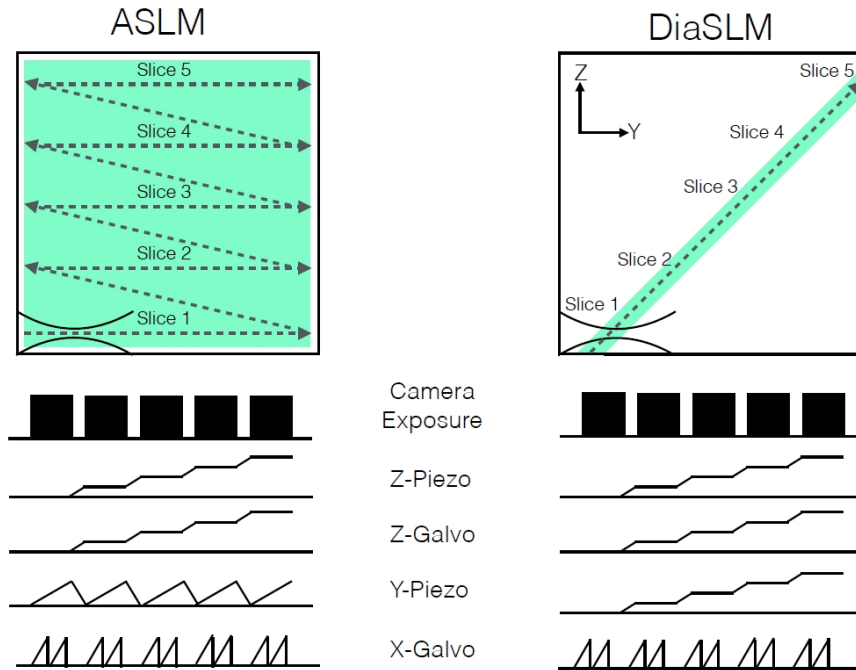
Figure S3. Schematic comparison of the beam scanning and camera control for ASLM and DiaSLM. In DiaSLM, the Y-piezo makes one complete cycle per image volume. In ASLM, the Y-piezo makes one complete cycle per image plane. Diagrams not to scale.
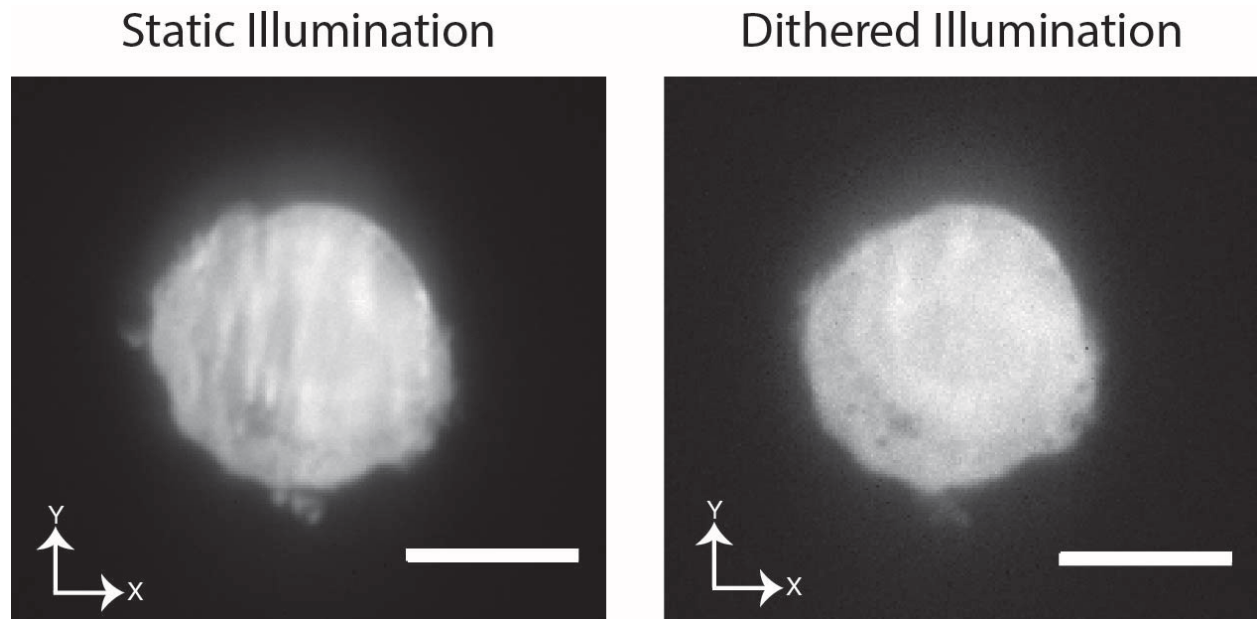

Figure S4. Improvement of illumination homogeneity by dithered Gaussian lattice. (Left) Static Gaussian illumination of an MV3 cell labeled with cytosolic GFP. (Right) Dithered Gaussian lattice illumination of the same cell. Scale bar 10 μm.
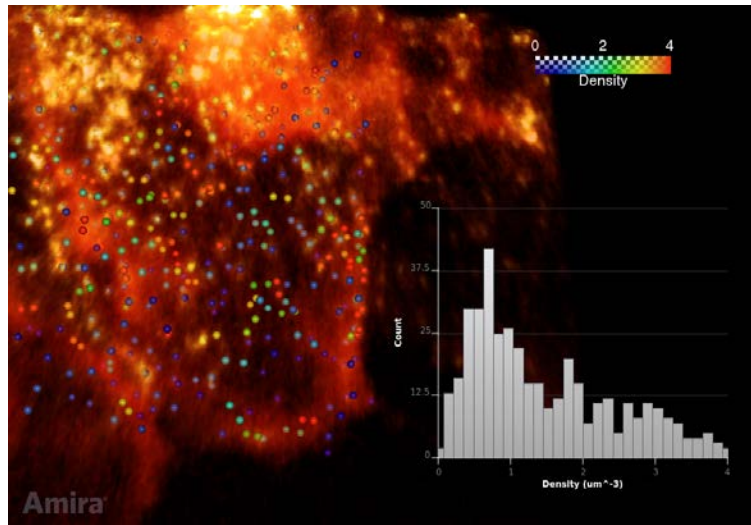
Figure S5. Density histogram (lower right), and locally measured density for each detected CLCa particle. The set of detected objects cover a volume of ~20x20x6 μm large.
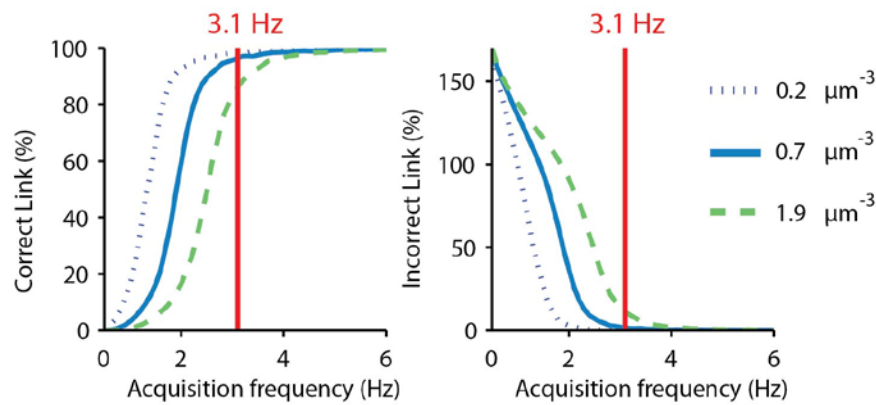

Figure S6. Tracking performance as a function of volumetric acquisition frequency on simulated dynamics of fast clathrin-associated structures (>2.22 μm/s) in a population of particles that simulate the density at the membrane (0.72 object per μm³). Performance is measured on tracks undergoing active transport only. Percentages are relative to the true number of correct links.
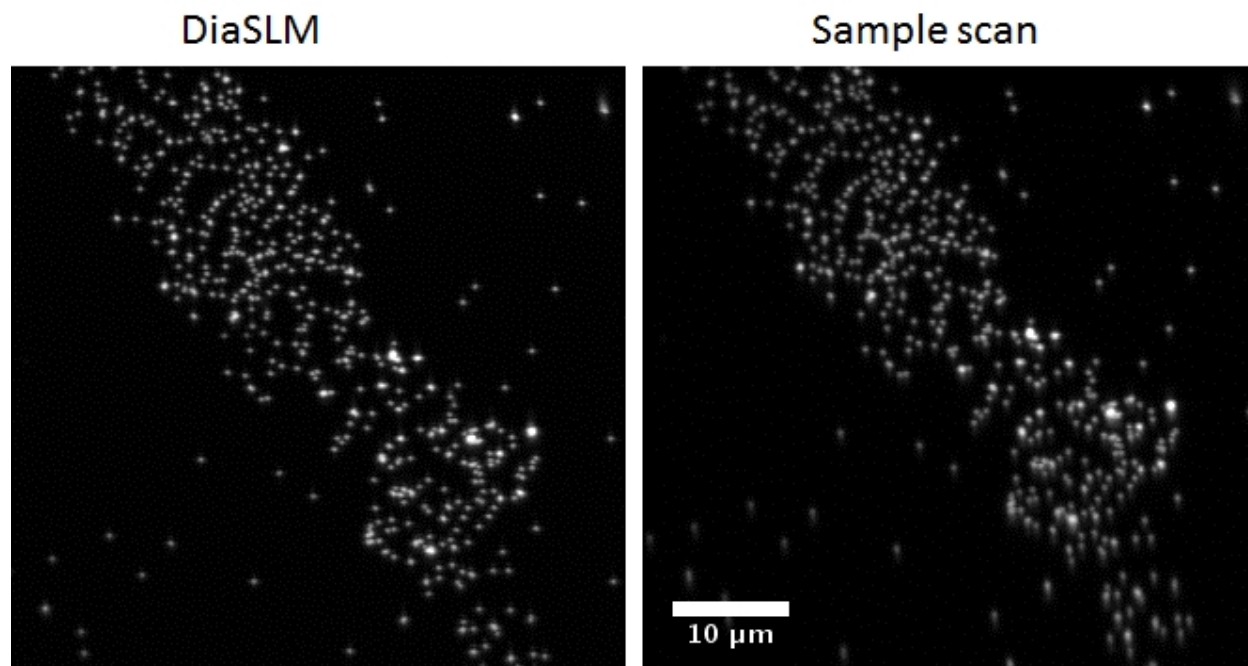
Figure S7. Comparison of DiaSLM and sample scanning. 200 nm fluorescent nanospheres were adhered to glass coverslips, and imaged with a 5 ms exposure time with (Left) DiaSLM and (Right) sample scanning. The two XZ images look comparable, except for the lower part of the sample scan image where the beads are slightly enlarged in the Z direction. However, the large scale oscillations that can be observed in the collagen imaging using sample scanning are not present.

Supporting Movies:
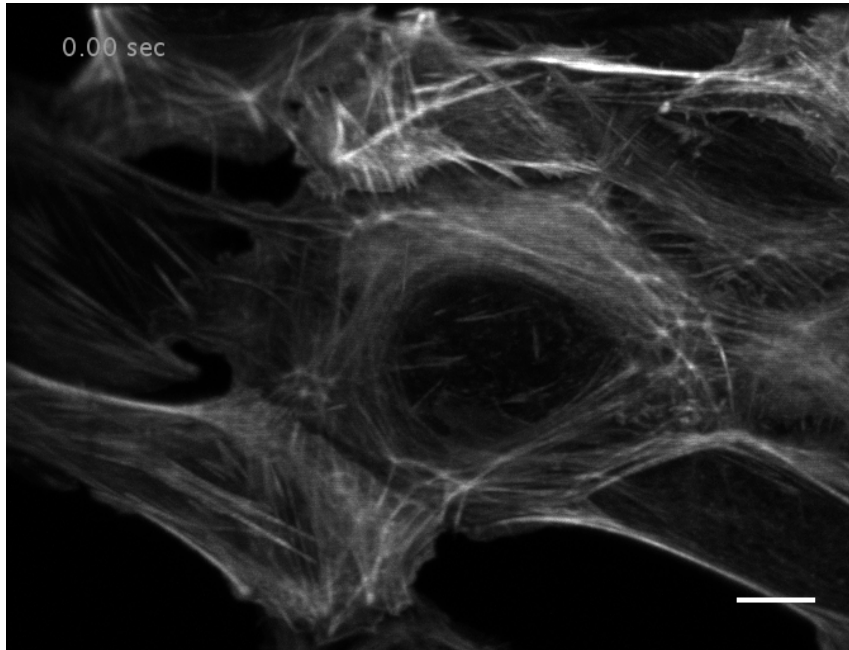
Movie S1. XY maximum intensity projection of F-actin dynamics in a monolayer of U2OS osteosarcoma cells, labeled with Tractin-CyOFP. Volumetric image acquisition rate of 0.37 Hz, 500 time points, 10 ms image acquisition per plane. Horizontal striping visible in the movie is likely due to laser intensity fluctuations. Scale bar 10 μm.
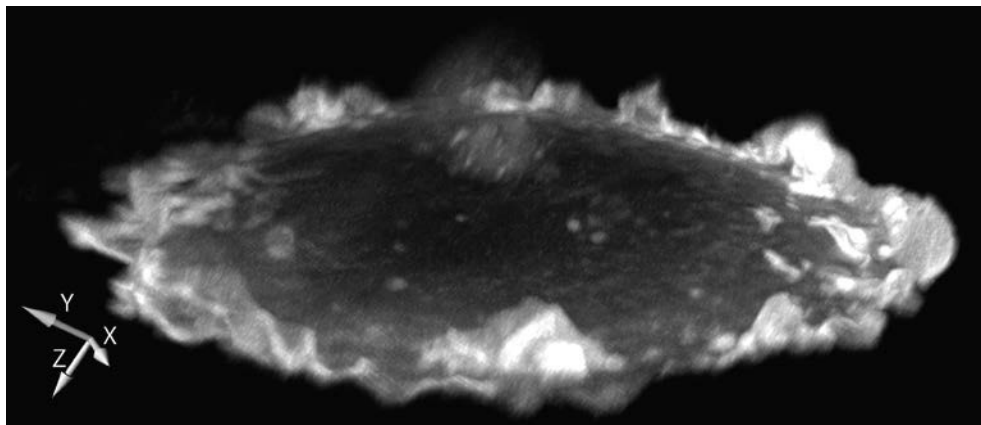
Movie S2. Volume rendering of a MV3 melanoma cell undergoing dynamic membrane ruffling, with enhanced phosphatidylinositol present in active membrane ruffles. Volumetric image acquisition rate of 0.37 Hz., 158 time points, 5 ms image acquisition per plane.
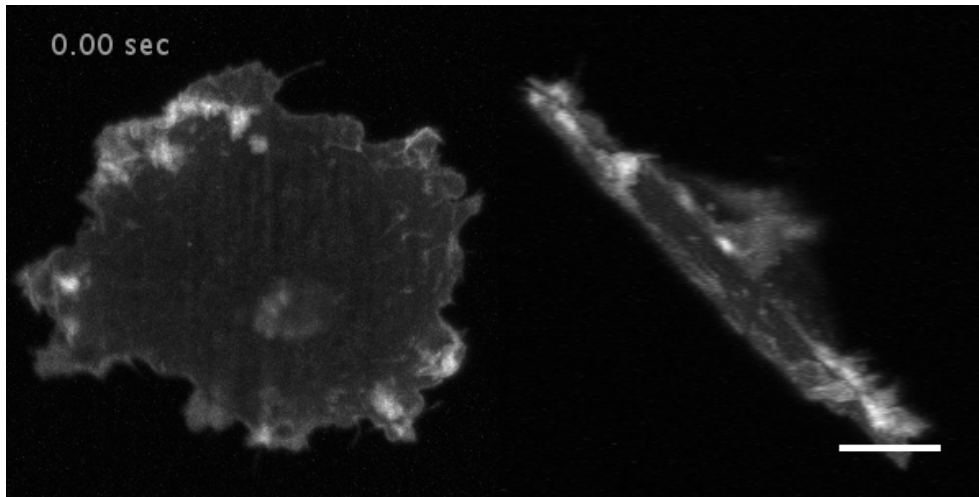
Movie S3. XY and ZY maximum intensity projections of an MV3 cell expressing AktPH-GFP. Volumetric image acquisition rate of 1 Hz, 500 time points, 5 ms image acquisition per plane. Scale bar 10 μm.
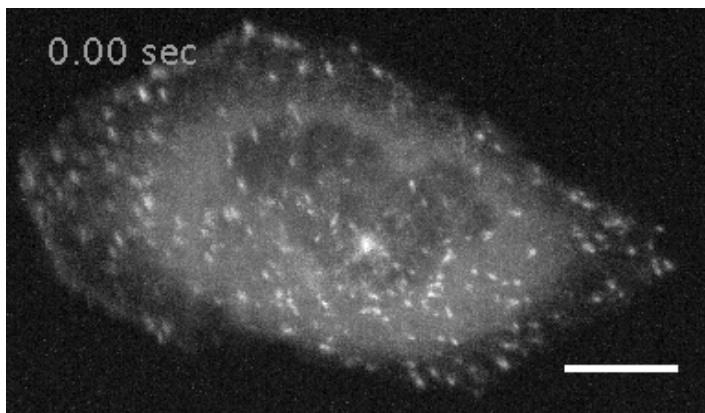
Movie S4. XY maximum intensity projection of microtubule +TIPs, labeled with EB3-mNeonGreen, in an osteosarcoma U2OS cell. Exponential photobleaching correction applied. Volumetric image acquisition rate of 0.46 Hz, 200 time points, 20 ms image acquisition per plane. Scale bar 10 μm.
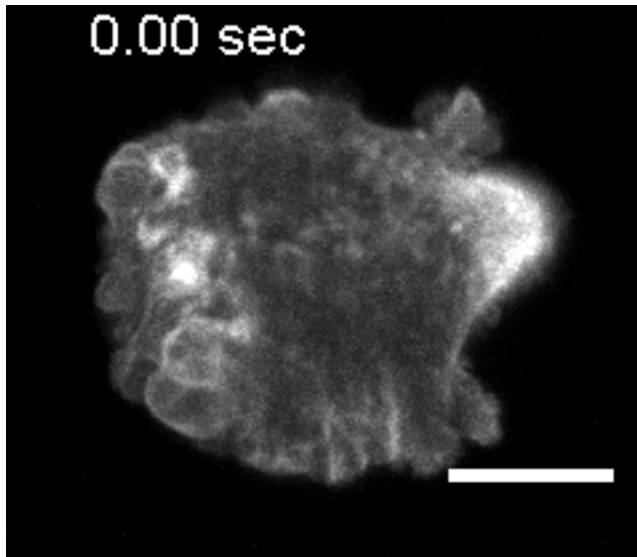
Movie S5. Polarized blebbing in a MV3 melanoma cell. XY maximum intensity projection of F-actin cytoskeleton imaged with Tractin-GFP. Volumetric image acquisition rate of 2.85 Hz., 1000 time points, 2.5 ms image acquisition per plane. Scale bar 10 μm.
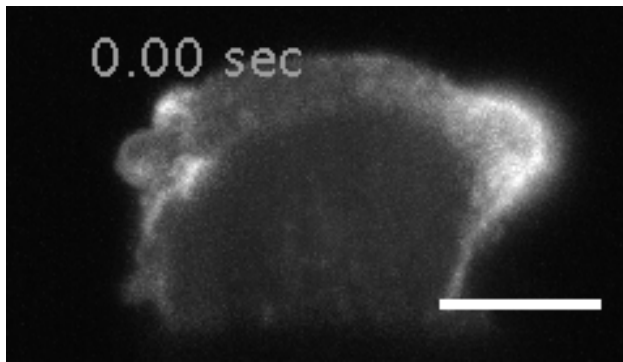
Movie S6. Cortical flow in polarized blebbing. Displayed as a local maximum intensity projection encompassing the central 4 μm of the cell. Same cell as in Movie S5. Volumetric image acquisition rate of 2.85 Hz., 1000 time points, 2.5 ms image acquisition per plane. Scale bar 10 μm.
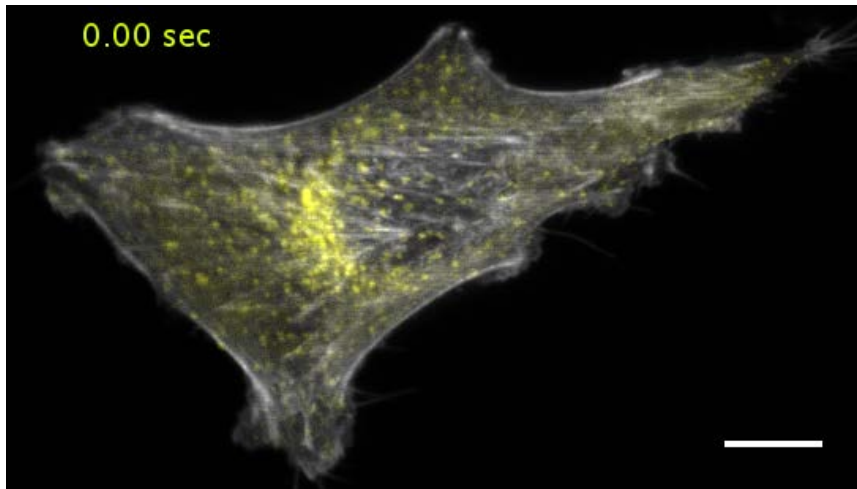
Movie S7. Clathrin-mediated endocytosis (yellow) and actin cytoskeleton (gray) dynamics in an SK-MEL2 melanoma cell. XY maximum intensity projection of clathrin light chain A (CLCa) marks active sites of endocytosis at the plasma membrane, and also labels intracellular structures associated with the Golgi apparatus, clearly visible in the perinuclear region of the cell. Each color channel acquired sequentially. Volumetric image acquisition rate of 0.20 Hz, 223 time points, 20 ms image acquisition per plane. Scale bar 10 μm.

Movie S8. XY maximum intensity projection of clathrin-mediated endocytosis (gray) and transferrin (yellow) uptake and intracellular transport in a human retinal pigment epithelial (ARPE-19) cell. Color channels are acquired simultaneously. Volumetric image acquisition rate of 0.36 Hz., 500 time points, 20 ms image acquisition per plane. Scale bar 10 μm.

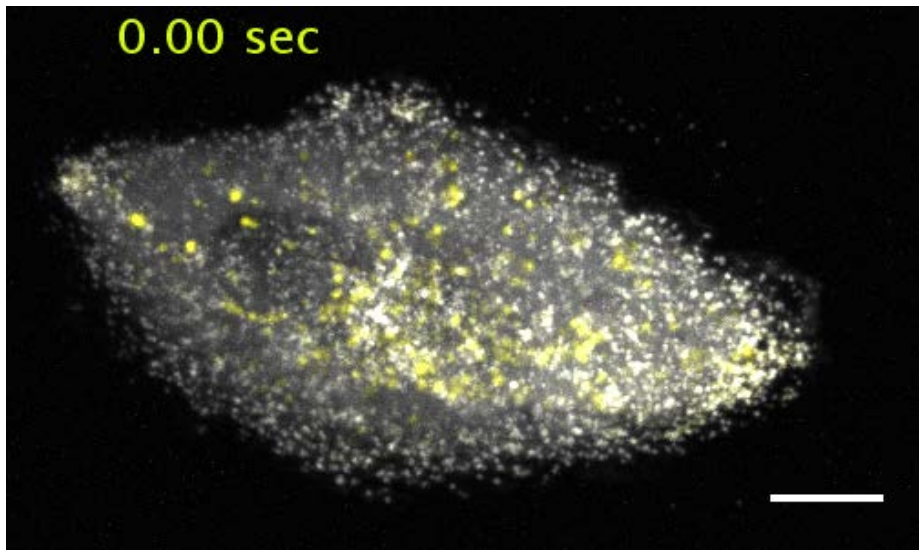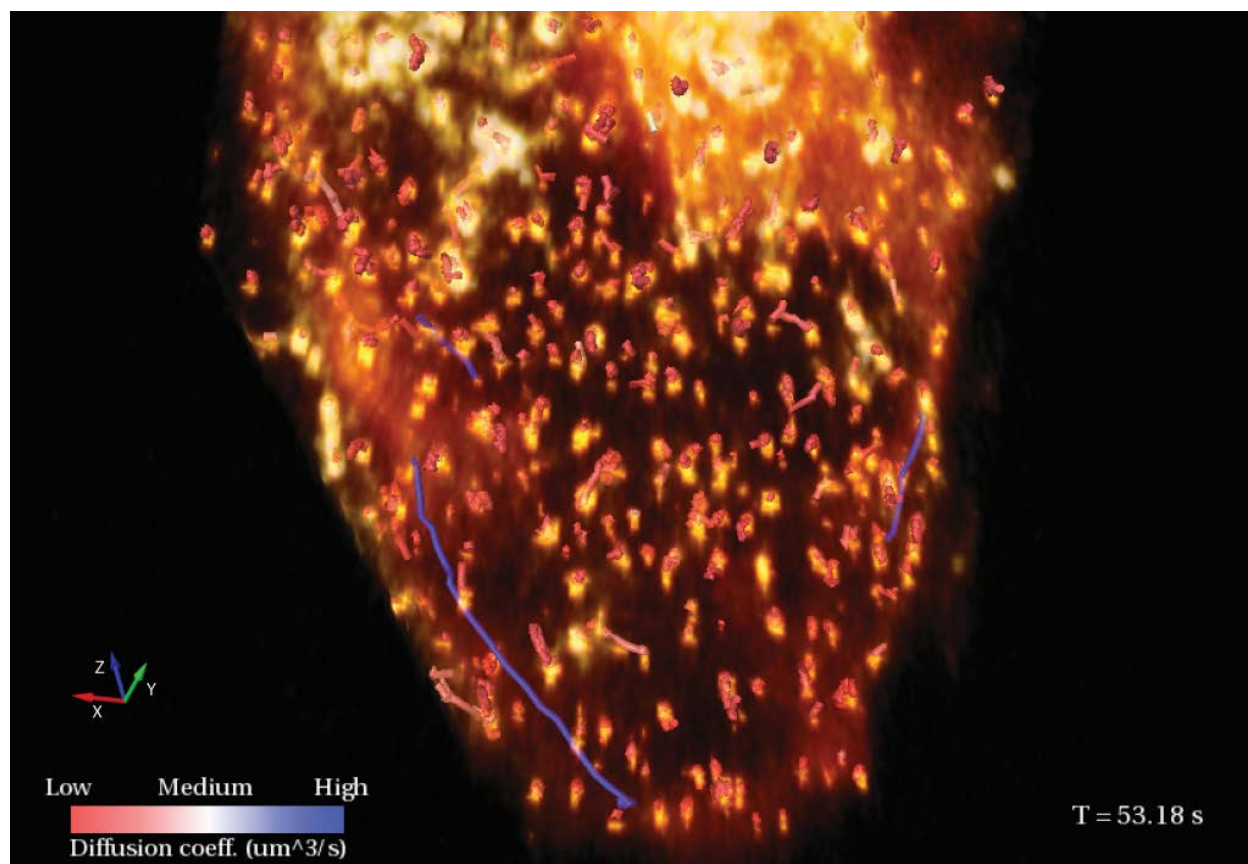**Movie S9**. 3D particle tracking of clathrin associated structures in Caco-2 human colon carcinoma cells at 3.5 Hz volumetric acquisition rate. The vast majority of tracks show a confined displacement at the membrane and thus exhibit a low diffusion coefficient (red colored tracks). Rare events of active translocations can be detected with a maximum velocity 4.5 μm/s (shown in blue).
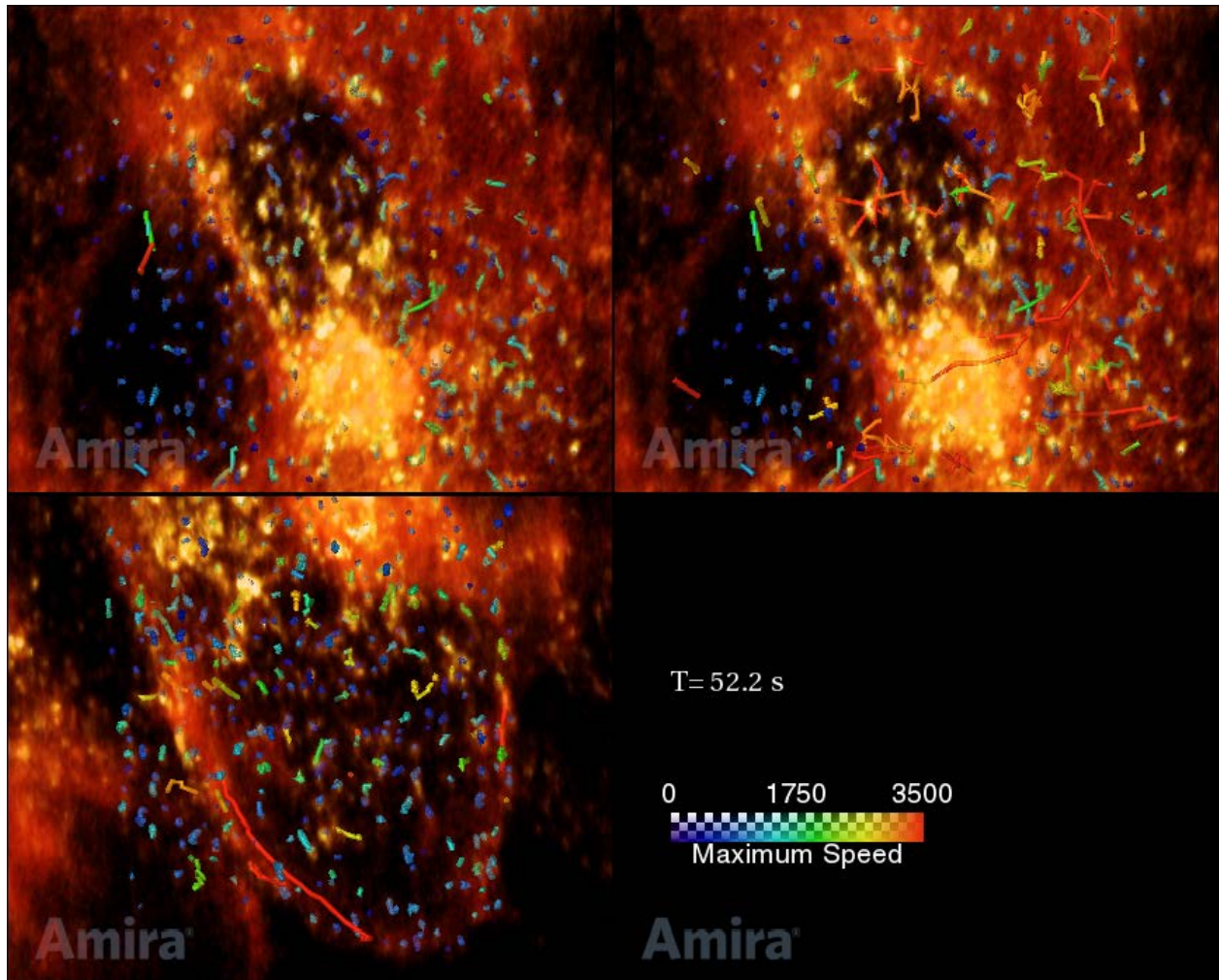
Movie S10: A minimum volumetric image acquisition rate of 3.1 Hz is necessary to accurately track 4.5 μm/s motion. Upper left, 2.2 Hz sequence tracked with a maximum search radius of 1.8 μm/s. Upper right: 2.2 Hz sequence tracked with a maximum search radius of 2.8 μm/s. Lower left: 3.5 Hz sequence tracked with a maximum search radius of 2.8 μm/s.
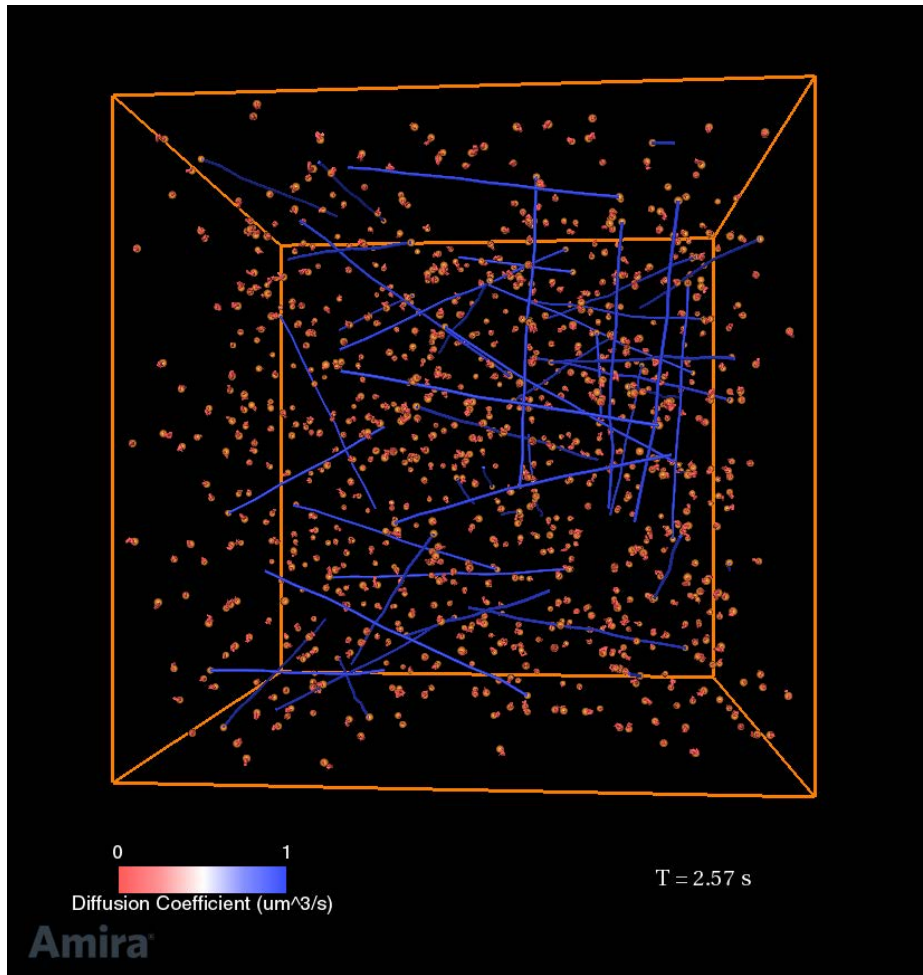
Movie S11: An example of simulated dynamics of intracellular clathrin-associated structures at the membrane (density is 0.72 object per μm^3). Tracks are pseudocolored using their estimated diffusion coefficient (red tracks are below 0.5 $\mu m^3/s$). Orange bounding box is 60x60x60 μm^3.
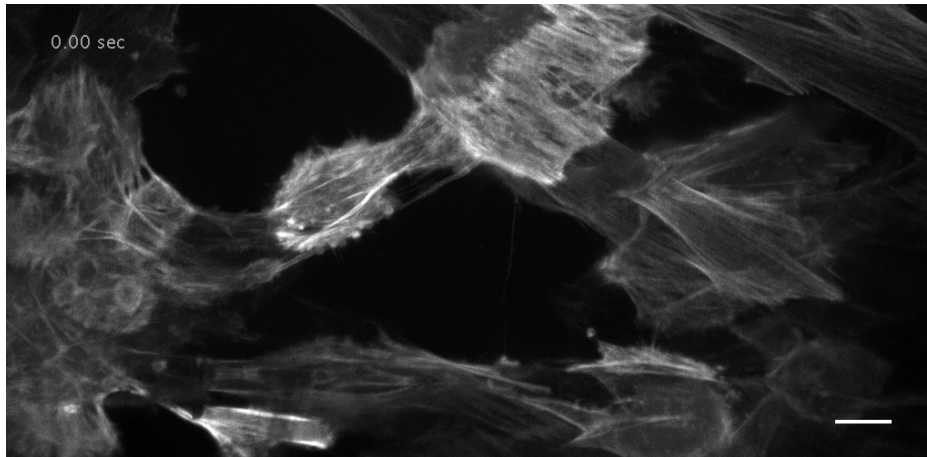
Movie S12. Human bronchial epithelial cells on a 50:50 extracellular matrix consisting of matrigel and type II collagen, 1 mg/mL. XY maximum intensity projection of cells labeled with Tractin-GFP. Volumetric image acquisition rate of 0.17 Hz., 500 time points, 10 ms image acquisition per plane. Scale bar 10 μm. Data has been subjected to image registration to account for movement of the sample using the ImageJ function StackReg.
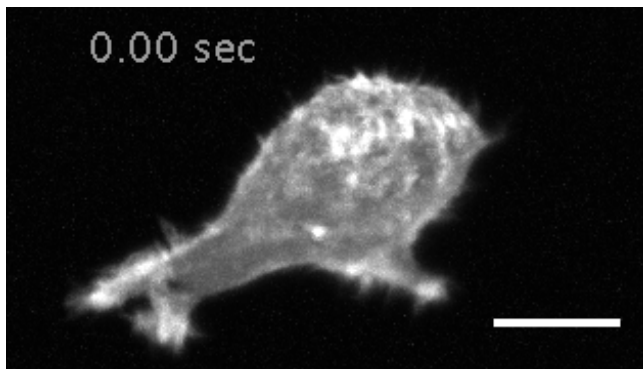
Movie S13. XY maximum intensity projection of human osteosarcoma U2OS cell undergoing cell spreading on a 2 mg/mL collagen matrix. Volumetric image acquisition rate of 1.37 Hz., 3000 time points, 2 ms image acquisition per plane.

Supporting Material

Supporting Note 1: 3D particle tracking.

The particle tracking approach is very similar to the one used in our previous report (1). We use the 3D version of the detector introduced by Auget *et al.* (2) and combine it with the u-track algorithm (3). A notable difference is the use of a multiple motion model to handle both confined Brownian displacement and directed displacement with multiple Kalman filters that compete with each other. Below are the parameters used for the tracking associated to the linking and the gap closing functions, respectively. The maximum search radius is set in voxels (normalized to the lateral voxel size), which was 800 or 1280 nm, depending on the experiment.

'costMatRandomDirectedSwitchingMotionLink'		'costMatRandomDirectedSwitchingMotionCloseGaps'	
LinearMotion	1	timeWindow	1
minSearchRadius	3	mergeSplit	0
maxSearchRadius	5 (or 8)	minTrackLen	3
brownStdMult	6	LinearMotion	0
useLocalDensity	0	minSearchRadius	2
nnWindow	timeWindow	maxSearchRadius	5
kalmanInitParam	[ ]	brownStdMult	6*timeWindow
		brownScaling	[0.25 0.01]
		ampRatioLimit	[0.7 4]
		LenForClassify	5
		useLocalDensity	0
		nnWindow	timeWindow
		maxAngleVV	[ ]
		gapPenalty	1.5

Supporting Note 2: Validation of acquisition frequency requirement with numerical simulations.

In order to cross-validate our experimental data showing the impact of volumetric acquisition frequency on automated tracking reliability (see Movie S10), we simulated imaging of intracellular transport in a dense environment. The synthetic dynamics reflect the active transport measured in our experimental datasets of clathrin vesicles (see Movie S11). As such, the population of synthetic particles undergoes active motions with a minimum speed of 2.2 μm/s in a dense field of locally confined diffusing particles. Acceleration is not simulated for the sake of simplicity. Consequently, the velocities of actively transported structures are modeled as stationary with an additional Brownian component. In our numerical experiments, we tune the frequency of acquisition and the particle density to evaluate automated tracking performance. The parameterization of our simulations is as follows:

- Volume: 100x100x100 μm
- Density: 0.1 to 4 particle/μm^3
- Active transport speed: 2.2 μm/s
- Active transport Brownian component: 0.01 μm^3/s
- Volume acquisition frequency : 1 to 6 Hz
- Confined motion proportion: 80%
- Active transport: 20%
- Frame number: 150
- Lifetime: follows a normal distribution with a mean and standard deviation of 10 and 25 seconds, respectively.
- Diffusion coefficient: 0.01 μm^3/s
- Confined radius: 0.3 to 0.8 μm (randomly distributed)

The parameters of the tracking algorithm are the same as in Note 1. The only difference is the upper bound of the frame-to-frame assignment radius (parameter maxSearchRadius) which adapts to the volumetric acquisition frequency from 2,200 nm/frames (for 1 Hz) down to 370 nm/frame (for 6 Hz). This provides us with a ground truth and a measured set of tracks with a finely tuned parameterization. By measuring the number of correct and wrong links estimated by the tracker and focusing on the directed displacement, we can evaluate the dynamic resolution of the simulated system in a systematic fashion.

To interrogate the impact of density and volumetric acquisition frequency on automated tracking performance, we simulated 12 different samples with intracellular densities ranging from 0.1 to 4 particles per volume. Fig. 5C shows that active transport of clathrin-associated structures cannot be reliably quantified below 3 Hz, even in the sparser scenario. These data also clearly show the large gap in efficiency between 2 Hz and 3 Hz.

We then tested the predictive power of our theoretical model (see Note 3) by simulating the median particle density measured at the membrane in our experimental sample (0.72 objects per μm^3) and measured the tracking performance against the acquisition frequency (see Fig. S7). As predicted by our model, the percentage of correct and incorrect links asymptotically reaches 100% and 0%, respectively, at a volumetric image acquisition frequency of ~ 3.1 Hz tracking. Fig. S7 also shows the impact of lower

acquisition frequencies on the measurements of particle dynamics for a specific density. At an image acquisition frequency of 2 Hz, the tracking quality deteriorates to 20%, underscoring the importance of high-speed 3D microscopes. These data also show that high particle densities (*e.g.*, adjacent to the Golgi apparatus) hinders particle tracking quality, suggesting that even faster microscopes may be needed for specific applications.

Supporting Note 3: Relationship between volumetric acquisition frequency and quantification of rapid intracellular transport.

For the quantification of rapid intracellular dynamics, it is intuitive that high frequency three-dimensional imaging is critical. However, it is currently unclear what improvements are required to capture the speeds and heterogeneity present in intracellular processes. In this supplemental note, we provide a simple model to estimate the required spatiotemporal resolution for a given acquisition setup for Brownian and directed displacement using state-of-the-art tracking techniques.

A typical tracking algorithm first detects particles in multiple image volumes, and then links the detected particles in a set of coherent tracks (4). If the apparent per-frame displacement of an object is fast and in a crowded environment, ambiguities arise in (i) the association of valid detections in neighboring trajectories, (ii) the inference of transient detection loss, (iii) the inference of false positives in the detection set, and (iv) the estimation of track termination and initiation. In an attempt to solve these problems, one strategy commonly used is to estimate the speed gating parameter, or "search radius" $S(t)$, which defines the maximum distance possible for one detected particle to be linked to another detected particle in the next frame. This parameter can be learned for each track, and adapted to accommodate new frames. However, it is usually saturated by a maximum value in an effort to avoid false positive links induced by the above-mentioned ambiguities (3, 4). Ideally, to allow for transient misdetection and spontaneous track initiation/termination, the sphere described by this search radius has a particle density below 1:

$$\frac{4}{3}\pi S(t)^3 d(t) < 1$$

where $d(t)$ is the local density. Obviously, this sphere should also contain all the possible motion of the object of interest. In the case of a freely diffusing particle we thus have:

$$\frac{v(t)}{f} < S(t)$$

where v is the instantaneous speed and f is the acquisition frequency. We can thus link the speed, acquisition speed and density with:

$$\frac{4}{3}\pi \left(\frac{|v(t)|}{f}\right)^3 d(t) < 1. \tag{1}$$

And the speed that can be estimated for given frequency and density:

$$|v| < f \sqrt[3]{\frac{3}{4\pi d(t)}}.$$

In the directed motion scenario, which is the most challenging in the CLCa experiment performed, an additional layer of complexity is added by the predictive capacity of Kalman filtering. After a first link, the Kalman filter estimates the trajectory

speed, allowing for a prediction of the particle location in the next frame. This prediction is then used for linking against candidate neighboring detection. U-track performs three tracking passes to estimate this speed. In turn, this means that condition (1) applies on the minimum speed of the track only, as far as the trajectories follow a quasi-stationary speed. Modeling speed variation through instantaneous acceleration a, directed transport is subject to the additional constraint:

$$\frac{4}{3}\pi\left(\frac{|a|}{f^2}\right)^3 d(t) < 1.$$

For a given density, the imaging frequency has a quadratic impact on the measurable acceleration.

Measuring local density on our experimental data, we can thus predict the speed attainable for a given acquisition frequency or, more importantly, knowing what acquisition frequency is required for a given magnitude of intracellular transport. Estimating local density according to the distance to the nearest neighbor, we find generally two modes: one at 0.72 object/μm^3 for sparser area and 1.9 object/μm^3 in the denser area, such as the Golgi apparatus (see also Fig. S6). This implies that for a conventional algorithm, an acquisition rate of 3.5 Hz should be able to capture speeds of up to 2.4 $\mu m/s$ in the Brownian case in the sparser area. As for directed transport, an acquisition rate of 3.5 Hz would enable us to reliably track trajectories that present a minimum speed of 2.4 $\mu m/s$ and instantaneous acceleration of 8.6 $\mu m/s^2$. Using an adaptive search radius that saturates at 800 nm/frame (2.8 $\mu m/s$), we can indeed measure directed motions as rapid as 4.5 $\mu m/s$ (see Fig. 5A and 5B) with our setup. The longest trajectory, on Fig. 5B, presents a minimum speed of 2.2 $\mu m/s$ in its directed section.

Our model predicts that the fastest trajectory measured in Fig. 5A, presenting a minimum speed of 2.2 $\mu m/s$ requires a minimum acquisition frequency of 3.1 Hz. In order to test the reliability of our model as well as verifying that our new microscope truly enables the capture of these displacements, we performed 2.3 Hz acquisition on the same cell type on the same day and under same conditions. While the SNR is noticeably better and thus detection more reliable, we observed a decrease in tracking quality. We performed automated tracking on this sequence using two different maximum search radius configurations. The first configuration saturates the search radius at 800 nm/frame, equivalent to a maximum speed of 1.8 $\mu m/s$ in the Brownian case. The second configuration saturates at 1200 nm/frame, to match the maximum speed set by the search radius set in our 3.5 Hz experiment (2.8 $\mu m/s$). The upper left panel in Movie S10 shows that the first configuration generates very few false positives, but fails to detect the fast motion captured at the 3.5 Hz acquisition speed in the lower left panel. The second tracking configuration results in very fast tracks that are clearly not endocytic structures (*i.e.,* their movement is incoherent and physically unlikely). These results are confirmed by our model. Theoretically, we should not be able to measure objects that go faster than 1.54 $\mu m/s$ in the Brownian case without false positives, and not be able to detect active transport are consistently above this speed and with acceleration above 3.4 $\mu m/s^2$. While trajectories that go as fast as 4.5 $\mu m/s$ are in theory within reach, they should then accelerate up to three times their lowest speed, reducing the number of potential candidates. For example, tracks similar to the longest one detected in Fig. 5A are not detectable with such a setup.

Supporting References:

1. Dean, Kevin M., P. Roudot, Erik S. Welf, G. Danuser, and R. Fiolka. 2015. Deconvolution-free Subcellular Imaging with Axially Swept Light Sheet Microscopy. Biophysical Journal 108:2807-2815.
2. Aguet, F., Costin N. Antonescu, M. Mettlen, Sandra L. Schmid, and G. Danuser. 2013. Advances in Analysis of Low Signal-to-Noise Images Link Dynamin and AP2 to the Functions of an Endocytic Checkpoint. Developmental Cell 26:279-291.
3. Jaqaman, K., D. Loerke, M. Mettlen, H. Kuwata, S. Grinstein, S. L. Schmid, and G. Danuser. 2008. Robust single-particle tracking in live-cell time-lapse sequences. Nature Methods 5:695-702.
4. Chenouard, N., I. Smal, F. de Chaumont, M. Maska, I. F. Sbalzarini, Y. Gong, J. Cardinale, C. Carthel, S. Coraluppi, M. Winter, A. R. Cohen, W. J. Godinez, K. Rohr, Y. Kalaidzidis, L. Liang, J. Duncan, H. Shen, Y. Xu, K. E. Magnusson, J. Jalden, H. M. Blau, P. Paul-Gilloteaux, P. Roudot, C. Kervrann, F. Waharte, J. Y. Tinevez, S. L. Shorte, J. Willemse, K. Celler, G. P. van Wezel, H. W. Dan, Y. S. Tsai, C. Ortiz de Solorzano, J. C. Olivo-Marin, and E. Meijering. 2014. Objective comparison of particle tracking methods. Nat Methods 11:281-289.